J. Fluid Mech. (2008), *vol.* 615, *pp.* 121–138. © 2008 Cambridge University Press
doi:10.1017/S0022112008003492 Printed in the United Kingdom

Azimuthal structure of turbulence in high Reynolds number pipe flow

SEAN C. C. BAILEY[1], MARCUS HULTMARK[1],
ALEXANDER J. SMITS[1] AND MICHAEL P. SCHULTZ[2]

[1]Department of Mechanical and Aerospace Engineering, Princeton University,
Princeton, NJ 08544, USA

[2]Department of Naval Architecture and Ocean Engineering, U.S. Naval Academy,
Annapolis, MD 21402, USA

(Received 26 November 2007 and in revised form 16 July 2008)

Two-point hot-wire measurements of streamwise velocity were performed in the logarithmic and wake regions of turbulent pipe flow for Reynolds numbers, based on pipe diameter, ranging from 7.6×10^4 to 8.3×10^6 at four wall-normal positions with azimuthal probe separation. The azimuthal correlations were found to be consistent with the presence of very large-scale coherent regions of low-wavenumber, low-momentum fluid observed in previous studies of wall-bounded flows and were found to be independent of changing Reynolds number and surface roughness effects. At the edge of the logarithmic layer the azimuthal scale determined from the correlations was found to be similar to that observed for channel flows but larger than that observed for boundary layers, inconsistent with the concept of a universal logarithmic region. As the wall-normal position increased outside the logarithmic layer, there was a decrease in azimuthal scale relative to that of channel flow. Using cross-spectral analysis, high-wavenumber motion was found to grow azimuthally with wall-normal distance at a faster rate than the low-wavenumber motions.

1. Introduction

Turbulent wall-bounded flows can be classified as being either external or internal, depending on the boundary conditions. Some of the simplest (and most widely studied) examples are the flat plate boundary layer, fully developed rectangular channel flow and fully developed pipe flow. The different boundary conditions create slightly different flow behaviour in each case; in zero-pressure-gradient boundary layers momentum is lost to wall shear, and the flow continuously develops streamwise, whereas (after sufficient development length) the streamwise pressure gradients in pipe and channel flows balance the wall shear, and the flow is fully developed. Differing boundary conditions also lead to differences in the structure of turbulence in the outer layer of the wall flow, the most prominent being the intermittency resulting from entrainment of irrotational free stream fluid into the boundary layer.

Recent flow visualizations, numerical studies and particle image velocimetry (PIV) investigations have expanded our knowledge of coherent structures in wall flows and demonstrated the existence of asymmetric and symmetric hairpin vortical structures (see for example Head & Bandyopadhyay 1981; Robinson 1991; Meinhart & Adrian 1995). These structures are believed to grow through merging with other hairpin structures of similar scale (Tomkins & Adrian 2003) with the oldest and largest structures extending as far as the wall layer height δ.

Single hairpin structures have also been observed to spawn trailing hairpin structures, which tend to travel at the same convective velocity (Zhou *et al.* 1999). Termed 'vortex packets', these groups of hairpin structures have a streamwise scale of approximately 2–3δ and have been associated with the bulges of turbulent fluid at the edge of the wall layer, also described as 'large-scale motions or LSMs', by Kim & Adrian (1999), Guala, Hommema & Adrian (2006) and Balakumar & Adrian (2007). The streamwise alignment of the hairpin structures within the packets induces long, narrow regions of low streamwise momentum (Adrian, Meinhart & Tomkins 2000; Ganapathisubramani, Longmire & Marusic 2003; Tomkins & Adrian 2003; Hutchins, Hambleton & Marusic 2005).

Very large-scale regions of low streamwise momentum more than 20δ long have also been observed in the logarithmic and wake regions of wall flows, although spanwise/azimuthal meandering of these regions makes it difficult to determine their typical streamwise extent (Hutchins, Ganapathisubramani & Marusic 2004; Hutchins & Marusic 2007*a*; Monty *et al.* 2007). Referred to as 'superstructures' (Hutchins & Marusic 2007*a*) or 'very large-scale motions (VLSMs)' (Kim & Adrian 1999; Tomkins & Adrian 2005; Guala *et al.* 2006; Balakumar & Adrian 2007) these structures are much longer than the sub-layer streaks and scale on outer variables. They are believed to be associated with the long streamwise modes observed in DNS data at large spanwise wavenumbers (Hoyas & Jiménez 2006). Although it has been proposed that these VLSMs are caused by pseudo-streamwise alignment of hairpin packets (Kim & Adrian 1999), it has also been suggested they could be formed by linear or nonlinear instabilities (e.g. Del Álamo & Jiménez 2006).

Spectral analysis of the VLSMs indicates that they have a non-negligible contribution to the turbulent kinetic energy and Reynolds stress production (Guala *et al.* 2006; Balakumar & Adrian 2007) which separate them from the inactive motions proposed by Townsend (1976). Careful analysis of DNS data has also revealed the footprint of the outer-scaled VLSM within the inner-scaled inner layer (Hoyas & Jiménez 2006; Hutchins & Marusic 2007*a*,*b*).

Most of the previous work investigating the spanwise scales of LSMs and VLSMs has concentrated on smooth-walled boundary layer and channel flows. However, the particular boundary conditions experienced in pipe flow may be expected to change the nature of the azimuthal scales of these motions. For example in channels and boundary layers the spanwise scale determined from the spanwise correlation (which contains contributions from both LSMs and VLSMs) increases monotonically with wall-normal position up to the maximum of δ or half the channel height, whereas geometrical considerations in pipe flow imply that spanwise scales cannot increase in the same way.

To investigate the azimuthal structure within pipe flow, Monty *et al.* (2007) used a rake of hot-wire probes and found that at the outer edge of the logarithmic region the azimuthal scale was nearly identical to that determined from similar measurements in channel flow. The measurements were confined to a single wall-normal position in the pipe, and hence the change in azimuthal scales with wall-normal distance could not be investigated.

Therefore, the objective of the current study is to investigate the wall-normal dependence of the azimuthal scale of the large-scale and very large-scale structures within the logarithmic and wake regions of pipe flow for a large range of Reynolds number based on pipe diameter D from $Re_D = 7.6 \times 10^4$ to $Re_D = 8.3 \times 10^6$, where $Re_D = D\langle U \rangle/\nu$; $\langle U \rangle$ is the area-averaged velocity, and ν is the kinematic viscosity. As well as providing the opportunity to investigate the Re_D dependence over a much

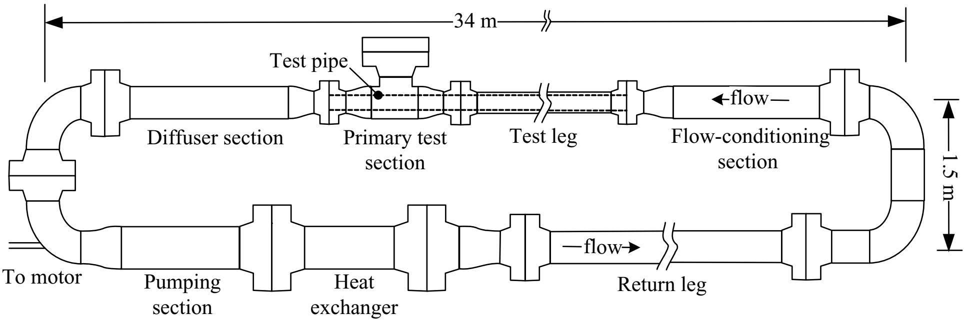

FIGURE 1. Schematic of experimental facility.

larger range of Reynolds numbers than previously studied for pipe flows, we will also examine the influence of wall roughness on large-scale and very large-scale features in the outer layer. In addition, the relationship between these large-scale and very large-scale features will be investigated using cross-spectral analysis.

2. Experiment description

2.1. *Experimental facility*

The experiments were conducted using the Princeton University/ONR Superpipe, which is described in detail by Zagarola (1996) and Zagarola & Smits (1998). The facility consists of a closed return-pressure vessel containing a long test pipe downstream of flow-conditioning and heat-exchanging sections (figure 1). By driving air compressed up to 200 atm through the test pipe, fully developed pipe flow is generated over a wide Reynolds number range, from 3.1×10^4 to 3.5×10^7.

For the current experiments the test section consisted of commercial steel pipe with an average inner diameter of 129.84 mm and an overall length of $200D$. The interior surface finish of the pipe had a root mean square roughness height of $k_{rms} = 5\,\mu\text{m}$. Its equivalent sand grain roughness k_s was $\simeq 1.6k_{rms}$. For further details see Langelandsvik, Kunkel & Smits (2008).

2.2. *Instrumentation*

Measurements were performed using two single-sensor hot-wire probes with platinum-plated tungsten wires of 2.5 µm diameter and 0.5 mm sensing length. Both probes were mounted onto a custom-designed traversing system positioned $196D$ downstream of the pipe inlet, with the probe sensors aligned in the azimuthal direction. The traversing system was designed such that a single probe could be positioned at a fixed wall-normal location, while a second probe at the same distance from the wall could be rotated to an arbitrary angular separation θ. The second probe was driven at a 1:1 gear ratio by a high-resolution (0.45° per step) stepper motor, located outside the test pipe and operated in half-step mode, resulting in an angular resolution of $\pm 0.23°$. At the wall-normal positions at which measurements were performed, the corresponding resolutions in probe separation were $1.8 \times 10^{-3}D$, $1.6 \times 10^{-3}D$, $1.4 \times 10^{-3}D$ and $9.8 \times 10^{-4}D$. The traverse geometry is illustrated in figure 2. Also shown are the orientations of the radial r and wall-normal directions y, the angular separation $\Delta\theta$ and azimuthal separation distance $\Delta s = r\Delta\theta$.

The frequency response of both probes was always greater than 65 kHz. The anemometer output was filtered at 30 kHz (fourth-order Butterworth filter) and

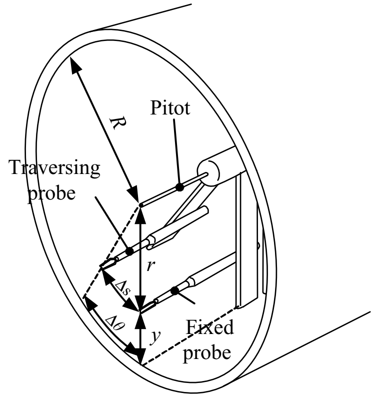

FIGURE 2. Experimental geometry and nomenclature.

digitized at 60 kHz using a 16-bit simultaneous sample and hold A/D board (National Instruments PCI-6123). Additional digital filtering at 10 kHz was performed during post-processing to eliminate electrical noise introduced by the traverse stepper motor. By comparing the data before and after digital filtering, it was concluded that no significant bias was introduced by this additional filtering.

Probe calibration was performed *in situ* before and after each measurement run using a Pitot probe located at the pipe centreline. The mean velocity at the probe radial position was determined from the mean centreline velocity, using the velocity profile and wall shear stress data of Langelandsvik *et al.* (2008) at identical flow conditions. Coefficients determined from least squares fit of the calibration data to King's law (using an exponent of 0.45) were then used to convert the measured bridge voltages to the effective velocity measured by the probe $U(t)$. When compared to previous results measured in the same facility under the same flow conditions, this calibration technique yielded second-order statistics that agreed within 10% in the worst case to the previously measured values.

To assess the uncertainty introduced by the traverse mechanism through flow blockage and eccentricity of the probe traverse path, the variation of the mean and fluctuating velocity components measured by the two probes was examined with changing Δs. Since the fixed probe should measure the same time-averaged statistics for all Δs, any changes in velocity statistics measured by this probe can be assumed to be caused by changes in the blockage introduced by the traversing apparatus. Furthermore, using the coarse assumption that the proximity of the probes to each other is the primary source of probe blockage (and thus blockage affects each probe approximately identically), an estimate of the magnitude of the eccentricity in the path of the traversing probe can be determined from the difference in time-averaged statistics when comparing the results from the two probes. The estimated combined uncertainty from the effects of traverse blockage and eccentricity is provided in figure 3.

To assess the possibility that the measurement apparatus distorted the structure of turbulence, the energy spectra measured by the two probes were compared at the minimum and maximum Δs. These auto-spectral densities, pre-multiplied using outer-layer scaling, are shown in figure 4 at $Re_D = 1.4 \times 10^6$ for each measured y/R. The form of the energy spectra does not depend on either the probe measurement position or which probe is performing the measurement. There is, however, some dependence of the amplitude of the energy spectra between the probes which could

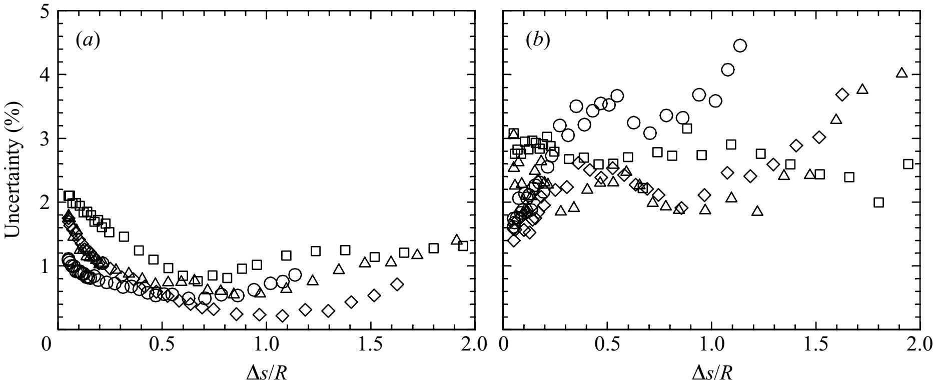

FIGURE 3. Estimated uncertainty in (*a*) mean velocity and (*b*) standard deviation of velocity because of combined effects of eccentricity and probe blockage at □, $y/R = 0.1$; △, $y/R = 0.2$; ◇, $y/R = 0.3$; ○, $y/R = 0.5$.

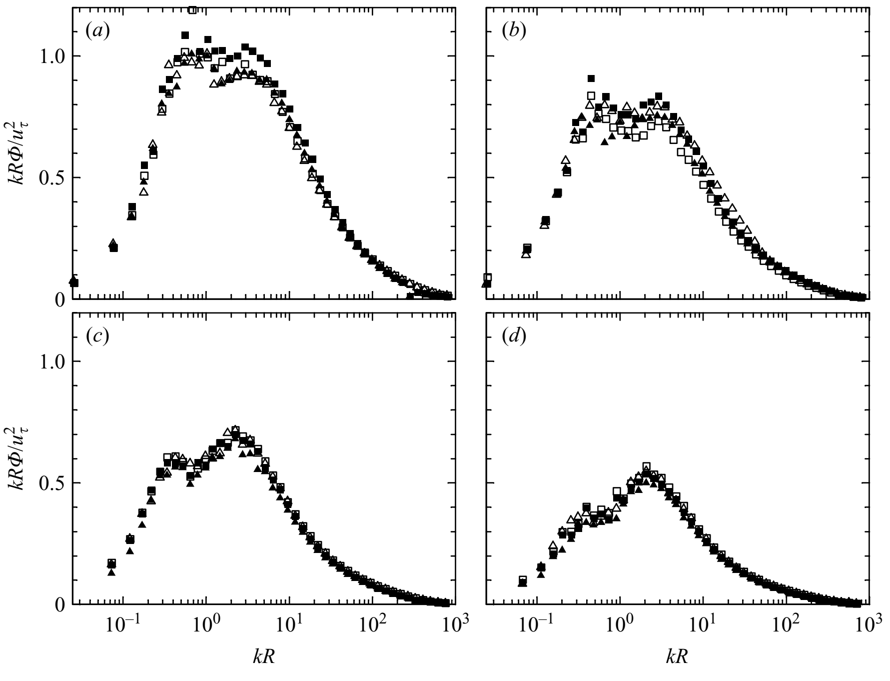

FIGURE 4. Pre-multiplied auto-spectral density $kR\Phi$ measured at $Re_D = 1.4 \times 10^6$ at minimum probe separation (□) and maximum probe separation (△) by fixed (hollow symbols) and traversing (filled symbols) probe at (*a*) $y/R = 0.1$, (*b*) $y/R = 0.2$, (*c*) $y/R = 0.3$ and (*d*) $y/R = 0.5$.

be attributed to the effects of traverse blockage and eccentricity. Since the azimuthal and wall-normal scales of the structures of interest in this study are on the order of $0.5R$, these small distortions in the flow field should not affect our conclusions regarding the behaviour of these structures.

2.3. *Measurement conditions*

Measurements were performed at $Re_D = 7.6 \times 10^4$ to 8.3×10^6, encompassing the hydraulically smooth, transitionally rough and fully rough flow regimes.

Re_D	Re_τ	$\langle U\rangle$ (m s^{-1})	δ_ν (μm)	k_s^+	λ	Flow type
7.6×10^4	1.9×10^3	8.98	40	0.2	0.0192	hydraulically smooth
1.5×10^5	3.4×10^3	17.5	20	0.4	0.0167	hydraulically smooth
5.2×10^5	1.1×10^4	16.3	6	1	0.0134	hydraulically smooth
1.4×10^6	2.7×10^4	15.1	2	3	0.0117	transitionally rough
2.8×10^6	5.2×10^4	16.9	1	6	0.0112	transitionally rough
5.5×10^6	1.0×10^5	17.3	0.6	10	0.0111	transitionally rough
8.3×10^6	1.6×10^5	19.9	0.4	20	0.0110	fully rough

TABLE 1. Experimental conditions: pipe Reynolds number Re_D, friction Reynolds number Re_τ, bulk velocity $\langle U\rangle$, viscous length scale δ_ν, equivalent sandgrain roughness $k_s^+=k_s/\delta_\nu$, friction factor λ and flow type.

Langelandsvik *et al.* (2008) determined the surface conditions to be transitionally rough for $1.4\lesssim k_s u_\tau/\nu\lesssim 18$ and fully rough for $k_s u_\tau/\nu\gtrsim 18$. Table 1 shows the flow parameters for each Reynolds number used in the current study.

At each Re_D, data were taken at four wall-normal positions: $y/R=0.1$, 0.2, 0.3 and 0.5. Based on the results of Langelandsvik *et al.* (2008), the measurement position of $y/R=0.1$ is considered to be within the log layer. Data at $y/R=0.2$ may be at the outer edge of the logarithmic region, although the outer boundary of the logarithmic region is difficult to define. The remaining two measurement locations are considered to be fully in the wake region. For each y/R, 180-s samples were taken with the traversing probe positioned at 31 to 33 azimuthal separations. Traverses were made unidirectionally from the minimum probe separation of $\Delta s=3.1$ mm (limited by the probe geometry) to the maximum angular separation allowed by the traverse geometry of $\Delta\theta=130°$.

3. Results and discussion

3.1. *Correlation coefficient*

Azimuthal profiles of the correlation coefficient were calculated according to

$$\rho(\Delta s)=\frac{\overline{u(0,t)u(\Delta s,t)}}{\sqrt{\overline{u^2(0,t)}}\sqrt{\overline{u^2(\Delta s,t)}}}, \tag{3.1}$$

where the overbar indicates a time average and $u=U-\overline{U}$. The resulting azimuthal profiles of correlation coefficient are presented in figure 5. The profiles are consistent with those previously reported for pipe, channel and boundary layer flows (see for example Hutchins *et al.* 2005; Monty *et al.* 2007). Most noticeable is the region of negative correlation occurring in the range $0.3\lessapprox\Delta s/R\lessapprox 1.3$ that is attributed to the coherent motions. Figure 5 shows that this negative region occurs for all measured y/R with the magnitude of the negative portion of the correlation at $y/R=0.1$, almost half that observed at $y/R=0.3$ and 0.5. As will be shown later, this change in the magnitude of negative ρ is caused by variations in the relative contribution of the VLSM and LSM to ρ. The correlations, and therefore the structures, are reasonably Re_D independent, as observed by Hutchins *et al.* (2005) for boundary layers and Monty *et al.* (2007) for pipe flows. They also appear to be relatively insensitive to roughness, consistent with the rough-wall boundary layer investigations of Wu & Christensen (2007) and Volino, Schultz & Flack (2007).

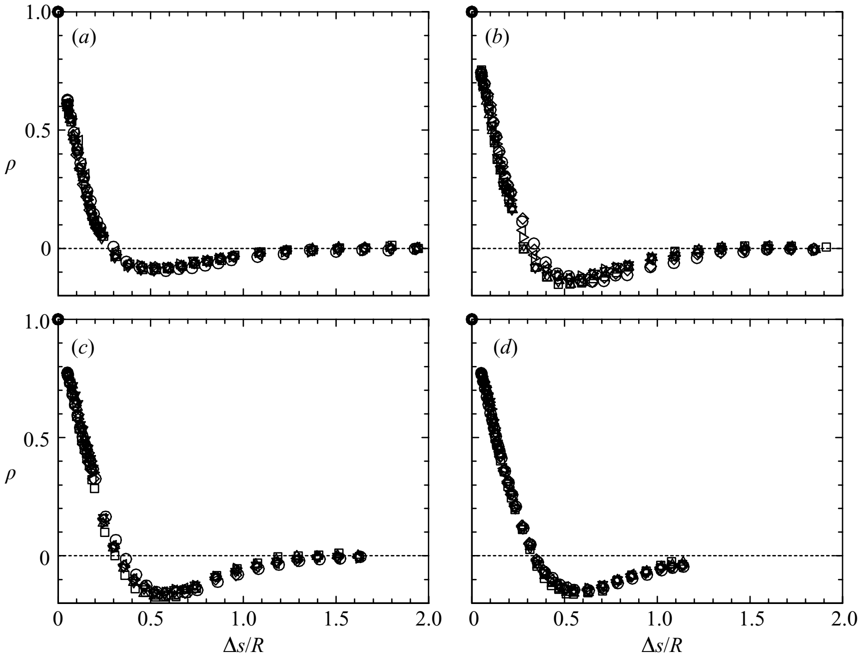

FIGURE 5. Correlation coefficient measured at (*a*) $y/R=0.1$, (*b*) $y/R=0.2$, (*c*) $y/R=0.3$ and (*d*) $y/R=0.5$; □, $Re_D=7.6\times10^4$; △, 1.5×10^5; ▽, 5.2×10^5; ▷, 1.4×10^6; ◁, 2.8×10^6; ◇, 5.5×10^6; ○, 8.3×10^6.

To visualize the variation of $\rho(\Delta s)$ with wall-normal position and to illustrate how the azimuthal scales relate to the pipe geometry, isocontours of $\rho(\Delta s)$ are shown in figure 6. This figure further illustrates the similarity of the azimuthal correlations over a Re_D range spanning two orders of magnitude and surface roughness conditions varying from hydraulically smooth to fully rough.

Ganapathisubramani *et al.* (2003) introduced a spanwise width scale l_z, defined as the range of spanwise displacement where $\rho(\Delta s)>0.05$, to help summarize such correlations as those shown in figure 5. The spanwise width scale determined from figure 5 is compared to previous measurements for boundary layer, channel and pipe flows in figure 7(*a*) (adapted from figure 6*a* in Monty *et al.* (2007) with additional data), where δ represents the height of boundary layer, half-height of the channel or pipe radius respectively.

Although there is considerable scatter, particularly at $y/R=0.2$, the spanwise width scales of the pipe and channel flows were found to be similar within the logarithmic layer, but both were twice that observed in the boundary layers. Note that, since the motions scale on outer variables, they therefore depend on the type of flow (boundary layer, channel or pipe). Also, the azimuthal scales contributing to l_z within the log layer are influenced by these outer-scale motions, resulting in a measurable contribution to the Reynolds stresses (Guala *et al.* 2006; Balakumar & Adrian 2007), so the differences observed in the scaling of l_z within the logarithmic layer are inconsistent with the notion that the turbulence structure within the logarithmic layer at high Reynolds numbers is universal.

For $y/R>0.2$, the azimuthal width in pipe flows decreases relative to the width observed in channel flows. This reflects the increased spatial constraints imposed in

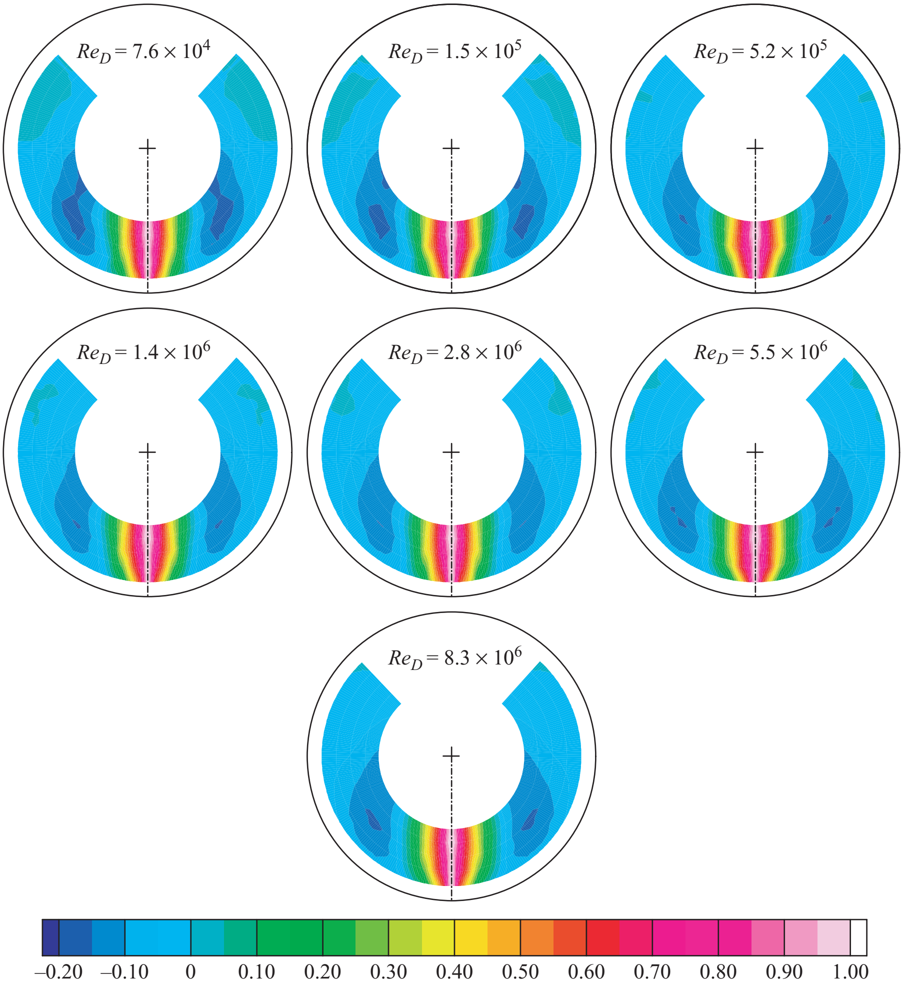

FIGURE 6. Isocontours of $\rho(\Delta s)$ for each Re_D investigated. The azimuthal range of the data is expanded by utilizing the even-functioned nature of 2-point correlations.

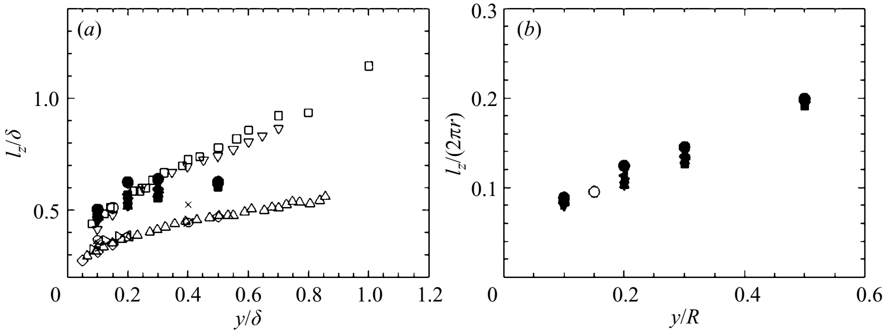

FIGURE 7. Dependence of the spanwise width scale l_z when (*a*) scaled by δ and (*b*) scaled by $2\pi r$. Here δ represents the height of boundary layer, half-height of the channel or pipe radius. Channel: □, Monty *et al.* (2007). Channel DNS: ▽, data of Del Álamo *et al.* (2004). Boundary layer: ▷, Tomkins & Adrian (2003); ◁, Krogstad & Antonia (1994); △, Hutchins *et al.* (2005); ◇, Hutchins & Marusic (2007*a*); ×, Volino *et al.* (2007). Rough-wall boundary layer: ∅, Volino *et al.* (2007). Pipe: ○, Monty *et al.* (2007). Present results: ■, $Re_D = 7.6 \times 10^4$; ▲, 1.5×10^5; ▼, 5.2×10^5; ►, 1.4×10^6; ◄, 2.8×10^6; ◆, 5.5×10^6; ●, 8.3×10^6.

pipe flow as y approaches R. The strong influence of geometry on the azimuthal scales is further illustrated in figure 7(*b*), which shows that when scaled by the local pipe circumference, l_z grows approximately linearly with y/R.

3.2. *Cross-spectra*

Two-point correlations, such as those shown in figure 5, contain contributions from motions over a wide range of scales which, through the averaging process, can obscure the azimuthal scale of LSMs and VLSMs. Hence, to investigate the dependence of the two-point correlations on streamwise wavenumber k, the one-sided cross-spectral density G, was calculated from

$$G(\Delta s, k) = F^{*}(0, k) F(\Delta s, k), \tag{3.2}$$

where F indicates the Fourier transform of the velocity signal, and * indicates a complex conjugate. Bendat & Piersol (2000) show that

$$\rho(\Delta s) = \int_0^\infty \mathrm{Re}[G(\Delta s, k)]\, \mathrm{d}k, \tag{3.3}$$

where Re indicates the real component. Thus, the quantity

$$\Psi(\Delta s, k) = \mathrm{Re}[G(\Delta s, k)] \sqrt{\overline{u^2(0, t)}} \sqrt{\overline{u^2(\Delta s, t)}} \tag{3.4}$$

can be defined such that $\Psi(0, k) = \Phi(k)$, the auto-spectral density measured by the fixed probe. Thus, $\Psi(\Delta s, k)$ can be thought of as the wavenumber distribution of the correlation coefficient at azimuthal separation Δs.

Isocontours of pre-multiplied cross-spectral density using outer layer scaling $kR\Psi$, are shown in figure 8 at $Re_D = 1.4 \times 10^6$ for each measured y/R. The corresponding pre-multiplied auto-spectra measured by the fixed probe are also shown. Only results at $Re_D = 1.4 \times 10^6$ are shown in figure 8, since similar results were observed at all Reynolds numbers.

The pre-multiplied auto-spectra in the current results are consistent with those previously reported by Kim & Adrian (1999). The most notable feature is the presence of two distinct peaks at $kR \approx 0.3 - 0.8$ and $kR \approx 2 - 5$, which have been attributed by Kim & Adrian (1999) to the distribution of VLSMs and LSMs respectively. For convenience, the terms VLSM and LSM will also be retained here to describe the motions at the corresponding spectral peak which will be considered to indicate the most common wavenumber of the motion. Although both peaks decrease in energy with increasing y/R, the energy contained in the VLSM peak decreases at a faster rate. Thus, within the logarithmic layer the VLSM peak is more prominent than the LSM peak, and within the outer layer the reverse is true.

The isocontours shown in figure 8 reveal a large region of negative Ψ within a range of Δs corresponding to the probe separation at which the negative values are observed in the cross-correlation results (figure 5). The azimuthal separations at which this negatively correlated region occurs decrease with increasing wavenumber.

At the measurement location closest to the wall, $y/R = 0.1$, the spanwise scale of the negatively correlated region shows no clear delineation between the VLSMs and LSMs, but there is a noticeable inflection point in the positively correlated values at approximately the same wavenumber as the inflection point in the corresponding auto-spectrum. The widest structures at this wall-normal position occur at streamwise wavenumbers associated with the VLSM peak. At this wavenumber, the negative Ψ values are centred at $\Delta s/R \approx 0.5$, which coincides with the azimuthal location of minimum $\rho(\Delta s)$ observed in figure 5 and by Monty *et al.* (2007). Thus, the present results clearly connect the streamwise VLSMs described by power-spectrum

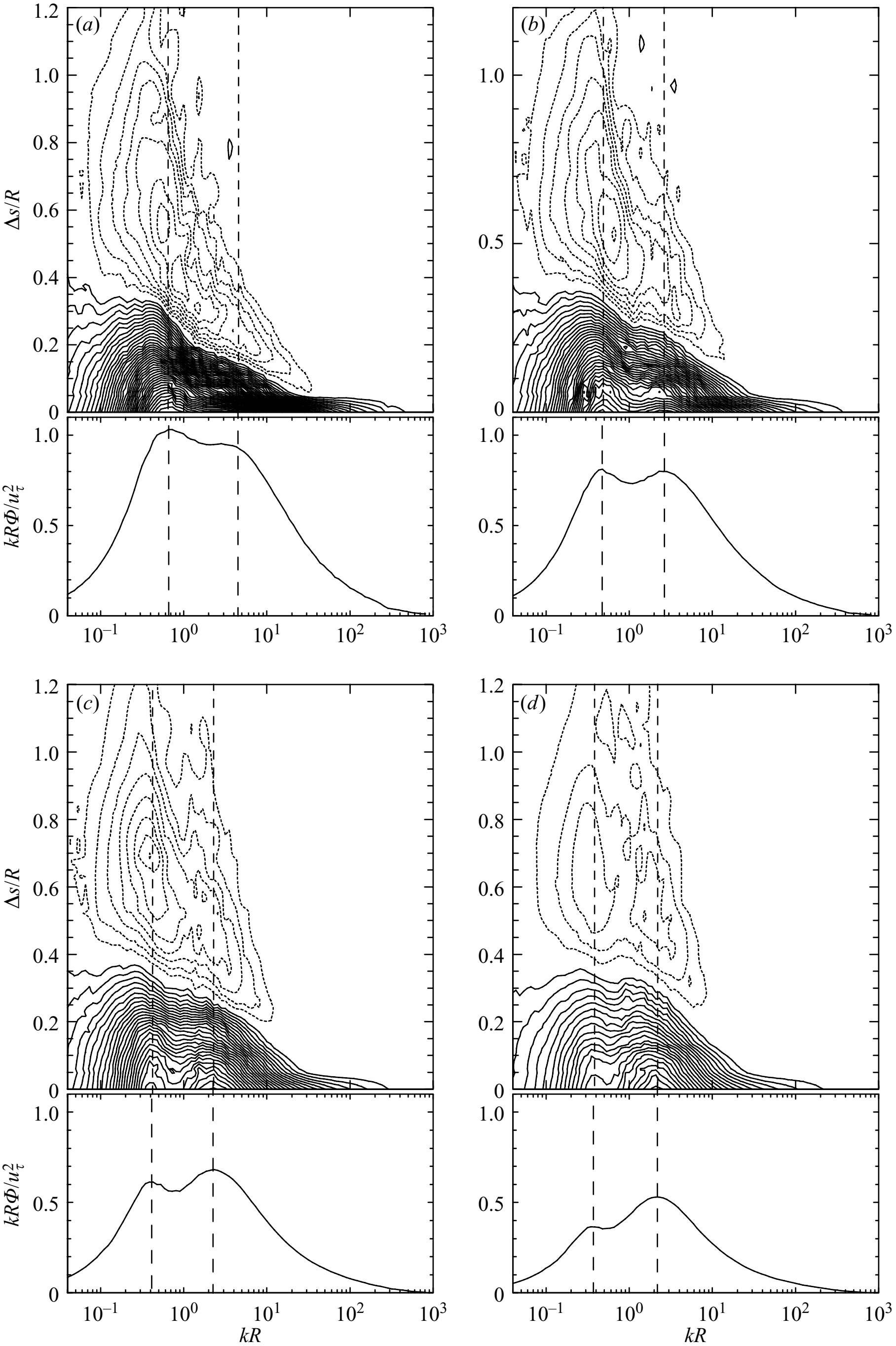

FIGURE 8. Contours of pre-multiplied cross-spectral density $kR\Psi/u_\tau^2$ at $Re_D = 1.4 \times 10^6$ for wall-normal locations (*a*) $y/R = 0.1$, (*b*) $y/R = 0.2$, (*c*) $y/R = 0.3$ and (*d*) $y/R = 0.5$. The contour levels are separated by 0.025; negative contours are shown as broken contour lines, and contour levels at zero are not shown for clarity. The corresponding pre-multiplied auto-spectral density $kR\Phi$ is shown below each contour plot. Wavenumbers of very large-scale and large-scale peaks indicated by dashed lines.

analysis (Kim & Adrian 1999; Guala *et al.* 2006; Balakumar & Adrian 2007) to the azimuthal/spanwise scale of 'superstructures' found using correlations and conditional averaging (see for example Hutchins & Marusic 2007*a*,*b*; Monty *et al.* 2007).

As wall distance increases, the energy contained within the VLSMs decreases relative to that contained within the LSMs. Correspondingly, the negatively correlated region at the LSM wavenumbers grows azimuthally and becomes distinct from that of the VLSM wavenumbers, resulting in the appearance of two separate regions of values negatively correlated by $y/R = 0.5$. Simultaneously, as y/R increases, the azimuthal scale at LSM wavenumbers approximately triples relative to the scale at LSM wavenumbers at $y/R = 0.1$, reflecting azimuthal growth of the LSM. For the same y/R range, the distribution of negative Ψ at VLSM wavenumbers appears to be independent of wall-normal distance.

An attempt to separate the contribution of the VLSM and LSM to ρ was made by spectral filtration of the cross-correlation, using

$$\rho_{vl}(\Delta s) = \int_0^{k_{cut}} \mathrm{Re}[G(\Delta s, k)]\, \mathrm{d}k, \tag{3.5}$$

where ρ_{vl} contains the contributions to ρ primarily from the VLSM, and

$$\rho_l(\Delta s) = \int_{k_{cut}}^{\infty} \mathrm{Re}[G(\Delta s, k)]\, \mathrm{d}k, \tag{3.6}$$

contains the contributions primarily from the LSM. The values of k_{cut} depend on wall-normal position and were selected using the location of the inflection in the corresponding auto-spectrum (as evident in figure 8). Here k_{cut} is considered to be a wavenumber below which the VLSM have the greatest energy contribution and above which the LSM have the greatest contribution. The selected values for $k_{cut}R$ were 1.5, 1.2, 0.8 and 0.6 for $y/R = 0.1, 0.2, 0.3$ and 0.5 respectively.

The resulting azimuthal distributions of ρ_{vl} and ρ_l for all measured wavenumbers are compared to the azimuthal distribution of ρ in figure 9. In general, the magnitude of ρ_{vl} is larger than that of ρ_l except at small very small Δs, where there is an increased contribution to ρ from small-scale motions. Figure 9 clearly shows differences in the azimuthal and wall-normal dependence of the VLSM and LSM. Figure 9 also highlights the observation that any width scale determined from the cross-correlation is not a good indicator of the width of either VLSM or LSM because the contribution of each type of motion to ρ varies with wall-normal position. At $y/R = 0.1$, where the VLSM has more energy than the LSM, the VLSM provides the greatest contribution to the cross-correlation, whereas at $y/R = 0.5$, the energy contained in the LSM relative to that contained in the VLSM increases to the point at which its corresponding contribution to ρ is approximately equal to that of the VLSM. Note that the increase in azimuthal width of the LSM, combined with the increased energy contained within them, causes the increase in the magnitude of the negative ρ values with the y/R observed in figure 5.

3.3. *Coherence function*

To further investigate and quantify the differences in behaviour of the azimuthal scale of the VLSMs and LSMs, a coherence function $\gamma(\Delta s, k)$ is introduced as

$$\gamma(\Delta s, k) = \frac{\Psi(\Delta s, k)}{\Phi^{1/2}(0, k)\Phi^{1/2}(\Delta s, k)}, \tag{3.7}$$

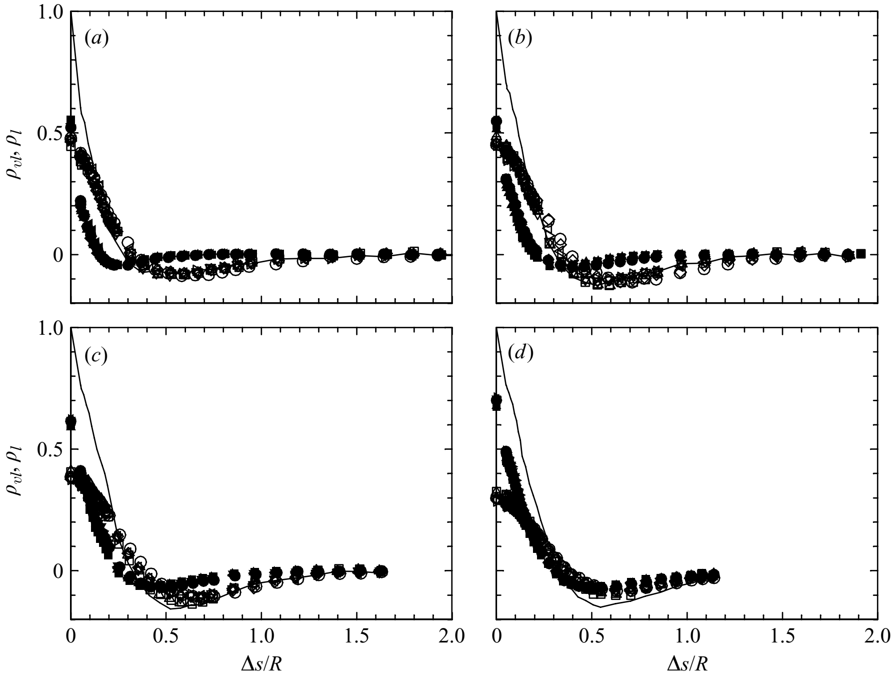

FIGURE 9. Comparison of azimuthal distributions of ρ_{vl} and ρ_l for (*a*) $y/R = 0.1$, (*b*) $y/R = 0.2$, (*c*) $y/R = 0.3$ and (*d*) $y/R = 0.5$. Symbols are as in figure 5 with hollow symbols used for ρ_{vl} and solid symbols for ρ_l. Solid line indicates correlation coefficient determined at $Re_D = 1.4 \times 10^6$ at corresponding wall-normal position.

where $\Phi(0, k)$ is the auto-spectrum measured by the stationary probe, and $\Phi(\Delta s, k)$ is the auto-spectrum measured by the traversing probe. Due to axi-symmetry, $\Phi(0, k) = \Phi(\Delta s, k)$ within experimental error (see figure 4). Note that γ retains the negative values of coherence, whereas the more commonly used coherency squared function utilizes the absolute value of the cross-spectrum, and hence the negative values of coherence are lost. These negative values of coherence are a useful indication of the existence and azimuthal scale of coherent structures.

This coherence function was used to compare the azimuthal scales of motion at the wavenumbers of the LSM and VLSM peaks, determined from the corresponding auto-spectrum as indicated by the broken lines in figure 8 for $Re_D = 1.4 \times 10^6$. Note that although the LSM and VLSM occur over a range of streamwise scales, the wavenumber at the peaks in the auto-spectrum were selected to characterize each type of motion. At the wavenumbers of the peaks, the corresponding motion is the most energetic, and its contribution to γ will therefore be the maximum. As shown for all Reynolds numbers in figure 10, these wavenumbers were found to be y/R dependent and qualitatively similar to the results of Kim & Adrian (1999) and Guala *et al.* (2006).

Figure 11 shows the azimuthal distribution of $\gamma(\Delta s, k)$ at the VLSM peak wavenumber. As could be expected from figures 8 and 9, the overall appearance of the γ distribution is very similar to that of $\rho(\Delta s)$ (shown in figure 11 using a solid line), but the magnitude of γ was found to be greater than $\rho(\Delta s)$ at the same azimuthal separation, reflecting the reduced influence on γ (when compared to ρ) by motions at streamwise scales other than that of the VLSM. Outside the logarithmic

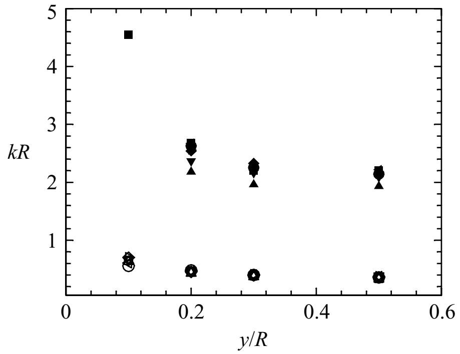

FIGURE 10. Wavenumbers of very large-scale peaks (hollow symbols) and large-scale peaks (solid symbols) determined from auto-spectra. Symbols are as in figure 5.

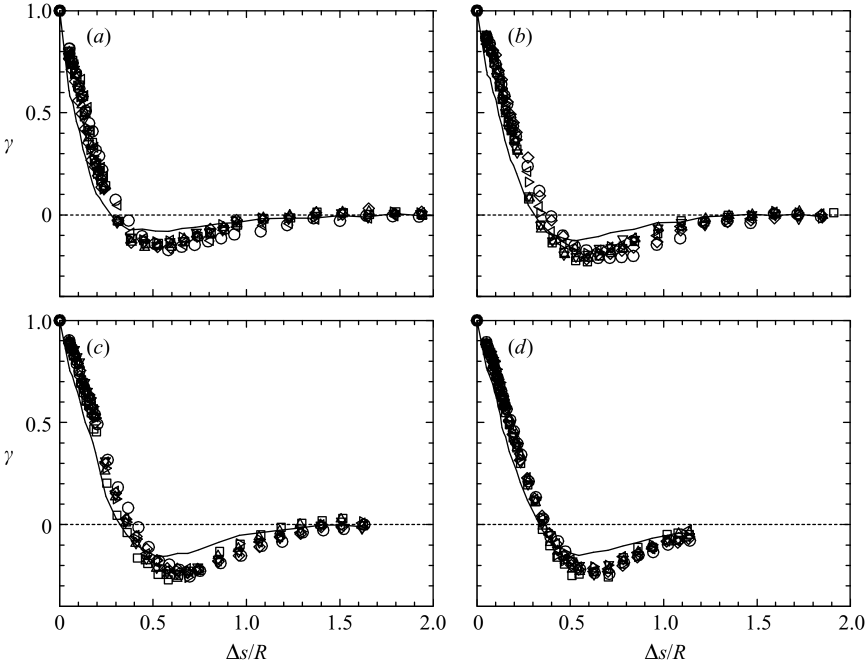

FIGURE 11. Azimuthal distribution of coherence function γ at VLSM wavenumbers measured at (*a*) $y/R = 0.1$, (*b*) $y/R = 0.2$, (*c*) $y/R = 0.3$ and (*d*) $y/R = 0.5$. Symbols are as in figure 5. Solid lines indicate azimuthal distribution of ρ at $Re_D = 1.4 \times 10^6$ for the corresponding y/R position.

layer ($y/R > 0.1$), there is very little change in the γ distributions with wall-normal distance, indicating little change in the azimuthal scale of the VLSM.

Figure 12 shows the azimuthal distribution of $\gamma(\Delta s, k)$ at the LSM peak in the auto-spectrum. Note that at $y/R = 0.1$, the LSM peak was not clearly defined for most of the Reynolds numbers (as evident in figure 8*a* for $Re_D = 1.4 \times 10^6$). Since the wavenumber of the LSM peak was found to show little Re_D dependence, at $y/R = 0.1$ the azimuthal distribution of γ for all Re_D values was determined at the LSM wavenumber found for $Re_D = 7.6 \times 10^4$, which had a clearly defined peak. The overall appearance of the azimuthal distribution of γ at the LSM peak wavenumber

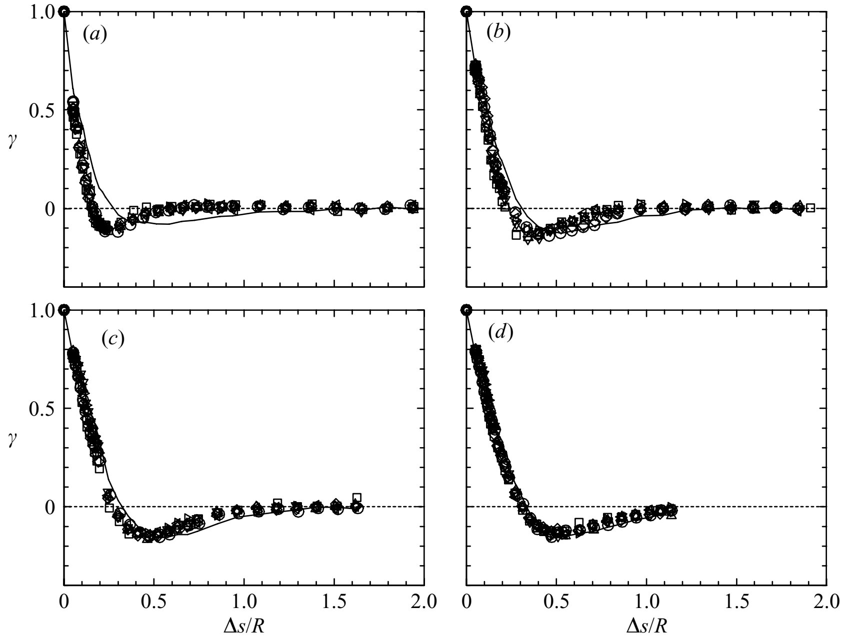

FIGURE 12. Azimuthal distribution of coherence function γ at LSM wavenumbers measured at (*a*) $y/R = 0.1$, (*b*) $y/R = 0.2$, (*c*) $y/R = 0.3$ and (*d*) $y/R = 0.5$. Symbols are as in figure 5. Solid lines indicate azimuthal distribution of ρ at $Re_D = 1.4 \times 10^6$ for the corresponding y/R position.

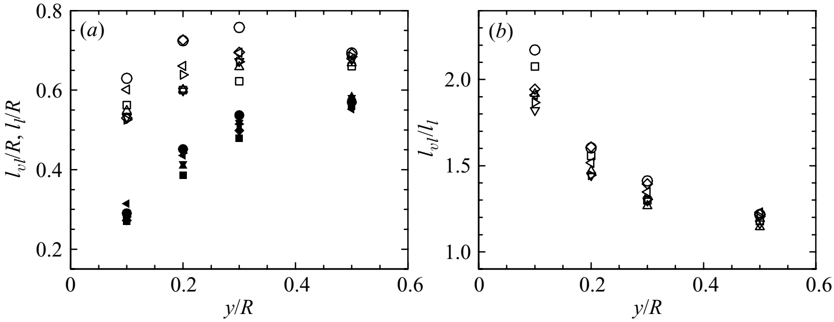

FIGURE 13. (*a*) Spanwise width scales l_{vl} and l_l as functions of y/R; hollow symbols l_{vl}; solid symbols l_l. (*b*) Ratio of l_{vl} to l_l. Symbols are as in figure 5.

in figure 12 is similar to that observed at the VLSM peak wavenumber shown in figure 11, although the magnitude of γ is reduced for the LSM. As also shown in figure 9 and unlike the previously noted behaviour of the VLSM, there is a strong y/R dependence evident for the LSM.

The y/R dependence of the azimuthal scale of the VLSM and LSM structures can be quantified and compared through definition of the spanwise width scales l_{vl} and l_l which, following the definition of l_z, are defined as the azimuthal separation over which $\gamma > 0.05$ at the VLSM and LSM peak wavenumber respectively. See figures 13(*a*) and 13(*b*). The azimuthal scale of the VLSM was found to be larger than the LSM at all y/R, but the ratio of their sizes decreases with wall distance: at $y/R = 0.1$, $l_{vl}/l_l \approx 2$, and at $y/R = 0.5$ the ratio decreases to about 1.2 (figure 13*b*).

This decrease in relative size is clearly due to the faster growth rate of the LSM with y/R (figure 13*a*). As the wall distance increases, however, the rate of growth of the LSM decreases, and l_{vl}/l_l appears to asymptote towards unity.

Previous researchers (see Zhou *et al.* 1999 for example) have observed that hairpin vortices can group into packets of streamwise aligned hairpins which travel at a common convection velocity. Within the logarithmic layer these hairpin packets can contain a wide range of scales, with only the oldest and largest of these structures persisting into the wake region, where they appear as turbulent bulges in the outer layer.

It has also been proposed that when these packets of hairpin vortices become streamwise aligned, they result in the very long, low-momentum regions of the superstructures/VLSMs (Kim & Adrian 1999; Adrian *et al.* 2000; Guala *et al.* 2006). If this were the case, it may be expected that the azimuthal scales of the LSMs and VLSMs would be similar at all wall-normal positions. The current results, however, show that the VLSMs are almost twice as wide as the LSMs at $y/R = 0.1$ and are still 25% larger at $y/R = 0.5$. This disparity of the spanwise scales is inconsistent with the streamwise alignment of several hairpin packets being the source of the VLSM, unless only the largest hairpin packets in the wake region ($y/R > 0.5$) align to produce the VLSM. In pipe flows, it would seem that the largest hairpin packets have a higher probability of alignment than the smaller packets because of increased azimuthal confinement at large y/R. The counter-rotating legs of these largest hairpin packets would then induce the VLSM at smaller y/R wall heights. This 'top-down' behaviour is supported by the outer scaling of the correlations and the relative insensitivity of the azimuthal correlations to the roughness conditions within the pipe. Hutchins & Marusic (2007*b*) have shown that the VLSM motions can be detected even within the buffer region. This influence of the outer-scaled VLSM near the wall could contribute to the poor scaling of the Re_D dependent near wall peak of $\overline{u^2}/u_\tau^2$ when scaled on inner variables (see Morrison *et al.* 2004 for example).

Such a top-down imposition of the VLSM could also explain the difference in azimuthal or spanwise scales within the logarithmic layer observed between the internal channel/pipe flows and the external boundary layer flows. As observed by Monty *et al.* (2007), for internal flows hairpin structures have been found to regularly project further into the outer layer than the boundary layers (Ganapathisubramani *et al.* 2003), which could result in azimuthally larger hairpin packets within the outer layer. This result would, in turn, create larger VLSMs. If alignment of these large-scale, outer-layer structures are the source of the VLSM, then the resulting VLSM imposed within the logarithmic layer can then be expected to be of wider scale for pipe/channel flows relative to the spanwise scale of the VLSM within the boundary layer.

Azimuthal meandering of the VLSM as observed by Hutchins & Marusic (2007*a*) and Monty *et al.* (2007) must also be considered when interpreting the results. Given sufficient magnitude, such meandering could cause the VLSM to appear wider in the cross-spectral analysis. This artificial increase in the azimuthal scales would have a greater effect on the VLSM relative to the LSM due to their longer streamwise length scale and hence would cause the VLSM to appear wider in time-averaged statistics. To investigate the potential influence of meander on the statistics, the synthetic eddy analysis of Hutchins & Marusic (2007*a*) was repeated using 200 ensembles of 50 structures having azimuthal width of $0.5R$ and normally distributed streamwise length scale of maximum length $20R$. Cross-correlations were calculated of synthetic eddy velocity fields with imposed peak to peak meandering amplitudes of $0R$, $0.5R$,

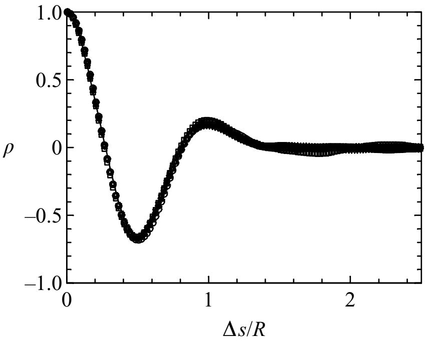

FIGURE 14. Azimuthal distribution of correlation coefficient determeined from synthetic velocity fields with peak-to-peak meandering amplitude of □, $0.5R$, △, $1R$, ▽, $1.5R$, ▷, $2R$, ◁, $3R$ and ○, $4R$ compared with the case with no meandering (solid line).

$1R$, $1.5R$, $2R$, $3R$ and $4R$. As shown in figure 14, there is a negligible effect on the cross-correlations, and it appears that the difference between the azimuthal scales of the VLSM and LSM cannot be attributed to wandering of the superstructures.

The disparity in wall-normal behaviour of the azimuthal scales of LSM and VLSM also supports the possibility that the LSM and VLSM are independent entities, suggesting that the VLSM could arise from nonlinear instabilities arising during transition to turbulence (Del Álamo & Jiménez 2006). Further support for this possibility is evident in the Reynolds number independence of the correlation coefficients (figure 5) and the slight positive correlation, reflecting possible periodicity, at large azimuthal separation and low Reynolds number seen in the isocontours of figure 6. Eckhardt *et al.* (2007) note that coherent structures arising from instabilities in transitional pipe flow can produce two to five low-speed streaks symmetrically arranged about the circumference of the pipe. The periodicity observed in figure 6 at $Re_D = 7.6 \times 10^4$ has a wavelength of approximately a third of the circumference, within the range cited by Eckhardt *et al.* (2007).

4. Conclusions

Two-point velocity measurements were performed over the Re_D range 7.6×10^4 to 8.3×10^6, spanning hydraulically smooth, transitionally rough and fully rough flow regimes. Over this range, little Re_D dependence was observed in the azimuthal correlation of streamwise velocity, in accordance with previous results for boundary layer and pipe flows (seen respectively in, Hutchins & Marusic 2007*a*; Monty *et al.* 2007). The azimuthal scale was also found to be independent of surface roughness, which is in accordance with the expectations based on Townsend's (1976) hypothesis.

Cross-spectral analysis of the velocity signals measured by the two probes indicated that the auto-spectral peaks associated with the VLSM and LSM by Kim & Adrian (1999), Guala *et al.* (2006) and Balakumar & Adrian (2007) were connected to the azimuthal and spanwise scales of the superstructures identified using cross-correlation and conditional averaging by Hutchins & Marusic (2007*a*,*b*) and Monty *et al.* (2007), amongst others.

At the outer edge of the logarithmic layer, the azimuthal width scale determined from azimuthal correlations of streamwise velocity showed good agreement with the values previously found in both channel and pipe flows. However the difference in the spanwise scale between the internal and external flows is inconsistent with the hypothesis that the structure of turbulence within the logarithmic region is universal.

In the wake region, the azimuthal width scale was found to be smaller than that of channel flows because of increased geometric confinement. The azimuthal scale of the LSM also increased with wall-normal distance, approaching that of the VLSM which remained comparatively constant within the uncertainty of the measurements as wall distance increased. This result indicates that if the VLSMs are caused by the streamwise alignment of packets of hairpin vortices, only the largest and oldest of these packets align to create these motions. Disparity between the azimuthal scales of the LSM and VLSM could support the possibility that the VLSM arise from linear or nonlinear instabilities within the turbulent flow.

The support of two ONR (Office of Naval Research) grants (program Manager Ron Joslin) is gratefully acknowledged. Additional support for S.C.C.B was provided by the Natural Sciences and Engineering Research Council of Canada through the postdoctoral fellowship program.

REFERENCES

Adrian, R. C., Meinhart, C. D. & Tomkins, C. D. 2000 Vortex organization in the outer region of the turbulent boundary layer. *J. Fluid Mech.* **422**, 1–54.

Balakumar, B. J. & Adrian, R. J. 2007 Large- and very-large-scale motions in channel and boundary-layer flows. *Phil. Trans. R. Soc.* A **365**, 665–681.

Bendat, J. S. & Piersol, A. G. 2000 *Random Data : Analysis and Measurement Procedures*. 3rd edn. Wiley Interscience.

Del Álamo, J. C. & Jiménez, J. 2006 Linear energy amplification in turbulent channels. *J. Fluid Mech.* **559**, 205–213.

Del Álamo, J. C., Jiménez, J., Zandonade, P. & Moser, R. D. 2004 Scaling of the energy spectra of turbulent channels. *J. Fluid Mech.* **500**, 135–144.

Eckhardt, B., Schneider, T. M., Hof, B. & Westerweel, J. 2007 Turbulence transition in pipe flow. *Annu. Rev. Fluid Mech.* **39**, 447–468.

Ganapathisubramani, B., Longmire, E. K. & Marusic, I. 2003 Characteristics of vortex packets in turbulent boundary layers. *J. Fluid Mech.* **478**, 35–46.

Guala, M., Hommema, S. E. & Adrian, R. J. 2006 Large-scale and very-large-scale motions in turbulent pipe flow. *J. Fluid Mech.* **554**, 521–542.

Head, M. R. & Bandyopadhyay, P. 1981 New aspects of turbulent boundary-layer structure. *J. Fluid Mech.* **107**, 297–337.

Hoyas, S. & Jiménez, J. 2006 Scaling of the velocity fluctuations in turbulent channels up to $Re_\tau = 2003$. *Phys. Fluids* **18**(1), 011702.

Hutchins, N., Ganapathisubramani, B. & Marusic, I. 2004 Dominant spanwise fourier modes and the existence of very large scale coherence in turbulent boundary layers. In *Proc. 15th Australasian Fluid Mechanics Conference*. Sydney, Australia.

Hutchins, N., Hambleton, W. T. & Marusic, I. 2005 Inclined cross-stream stereo particle image velocimetry measurements in turbulent boundary layers. *J. Fluid Mech.* **541**, 21–54.

Hutchins, N. & Marusic, I. 2007*a* Evidence of very long meandering features in the logarithmic region of turbulent boundary layers. *J. Fluid Mech.* **579**, 1–28.

Hutchins, N. & Marusic, I. 2007*b* Large-scale influences in near-wall turbulence. *Phil. Trans. R. Soc.* A **365**, 647–664.

Kim, K. C. & Adrian, R. J. 1999 Very large-scale motion in the outer layer. *Phys. Fluids* **11** (2), 417–422.

Krogstad, P. Å & Antonia, R. A. 1994 Structure of turbulent boundary layers on smooth and rough walls. *J. Fluid Mech.* **277**, 1–21.

Langelandsvik, L. I., Kunkel, G. J. & Smits, A. J. 2008 Friction factor and mean velocity profiles in a commercial steel pipe. *J. Fluid Mech.* **595**, 323–339.

MEINHART, C. D. & ADRIAN, R. J. 1995 On the existence of uniform momentum zones in a turbulent boundary layer. *Phys. Fluids* **7** (4), 694–696.

MONTY, J. P., STEWART, J. A., WILLIAMS, R. C. & CHONG, M. S. 2007 Large-scale features in turbulent pipe and channel flows. *J. Fluid Mech.* **589**, 147–156.

MORRISON, J. F., MCKEON, B. J., JIANG, W. & SMITS, A. J. 2004 Scaling of the streamwise velocity component in turbulent pipe flow. *J. Fluid Mech.* **508**, 99–131.

ROBINSON, S. K. 1991 Coherent motions in turbulent boundary layers. *Annu. Rev. Fluid Mech.* **23**, 601–639.

TOMKINS, C. D. & ADRIAN, R. J. 2003 Spanwise structure and scale growth in turbulent boundary layers. *J. Fluid Mech.* **490**, 37–74.

TOMKINS, C. D. & ADRIAN, R. J. 2005 Energetic spanwise modes in the logarithmic layer of a turbulent boundary layer. *J. Fluid Mech.* **545**, 141–162.

TOWNSEND, A. A. 1976 *The Structure of Turbulent Shear Flow*. 2nd edn. Cambridge University Press.

VOLINO, R. J., SCHULTZ, M. P. & FLACK, K. A. 2007 Turbulence structure in rough- and smooth-wall boundary layers. *J. Fluid Mech.* **592**, 263–293.

WU, Y. & CHRISTENSEN, K. T. 2007 Outer-layer similarity in the presence of a practical rough-wall topography. *Phys. Fluids* **19** (8), 085108.

ZAGAROLA, M. V. 1996 Mean-flow scaling of turbulent pipe flow. PhD thesis, Princeton University, Princeton, NJ, USA.

ZAGAROLA, M. V. & SMITS, A. J. 1998 Mean-flow scaling of turbulent pipe flow. *J. Fluid Mech.* **373**, 33–79.

ZHOU, J., ADRIAN, R. J., BALACHANDAR, S. & KENDALL, T. M. 1999 Mechanisms for generating coherent packets of hairpin vortices in channel flows. *J. Fluid Mech.* **387**, 353–396.